AIAA JOURNAL
Vol. 45, No. 11, November 2007

# High-Resolution Computational and Experimental Study of Rotary-Wing Tip Vortex Formation

Karthikeyan Duraisamy,* Manikandan Ramasamy,* James D. Baeder,† and J. Gordon Leishman‡
*University of Maryland, College Park, Maryland 20742*

DOI: 10.2514/1.26575

**The formation and rollup of a tip vortex trailed from a hovering helicopter rotor blade is studied in detail using both computations and measurements. The compressible Reynolds-averaged Navier–Stokes equations are computationally solved on an overset mesh system. The flow measurements are made using stereoscopic particle image velocimetry. The high resolution of both the numerics and the measurements reveal multiple coherent structures in the evolving rotor tip vortex flowfield. Secondary and tertiary vortices that result from crossflow separations near the blade tip are identified. These vortices, along with a part of the trailed wake, are ultimately entrained into the tip vortex that is formed downstream of the blade's trailing edge. The simulations clearly demonstrate the resolution required to accurately represent the complex three-dimensional flowfield. The advantage of particle image velocimetry, which has the ability to make planar measurements at a given instant of time, has been fully used to validate the computational fluid dynamics predictions. Even though linear eddy viscosity models are expected to inadequately represent the details of the turbulent quantities, good agreement is seen to be achieved with the particle image velocimetry measurements of the mean flowfield. The various sources of computational and measurement uncertainties are discussed.**

## Nomenclature

| | | |
|---|---|---|
| $C_L$ | = | local lift coefficient, sectional lift/$\frac{1}{2}\rho c\Omega R^2$ |
| $C_T$ | = | coefficient of thrust, rotor thrust/$\pi\rho\Omega^2 R^4$ |
| $c$ | = | blade chord, m |
| $M$ | = | sectional Mach number |
| $R$ | = | radius of the rotor blade, m |
| $r$ | = | vortex radial coordinate, m |
| $r_c$ | = | core radius of the tip vortex, m |
| $x, y, z$ | = | particle image velocimetry coordinates, m |
| $V_{\text{ax}}$ | = | axial velocity of the tip vortex, m/s |
| $V_\theta$ | = | swirl velocity of the tip vortex, m/s |
| $\rho$ | = | density of air, kg/m$^3$ |
| $\sigma_{\text{swirl}}$ | = | scatter in the swirl velocity magnitude, m/s |
| $\sigma_{\text{axial}}$ | = | scatter in the axial velocity magnitude, m/s |
| $\psi$ | = | wake age, deg |
| $\Omega$ | = | angular velocity of the blade, rad/s |
| $\omega$ | = | magnitude of the vorticity tensor, s$^{-1}$ |

## Introduction

SCIENTIFIC interest in understanding the formation and evolution of tip vortices from rotating wings continues because of their substantial influence on the overall performance of the rotor system. This is especially true when the rotor operates under certain conditions such as descending flight, in which the tip vortices trailing from one blade interact with the following blades. This leads to substantial unsteady airloads, noise, and vibration. In hovering flight, the persistence of tip vortices, combined with their spatial proximity to the rotor blades, means that the tip vortices induce a significant flow velocity on the rotor blades. Therefore, developing a better knowledge on the formation and evolutional characteristics of the tip vortices becomes important if the final goal is to have an efficient, quiet helicopter.

Received 16 July 2006; revision received 2 March 2007; accepted for publication 17 March 2007. Copyright © 2007 by the American Institute of Aeronautics and Astronautics, Inc. All rights reserved. Copies of this paper may be made for personal or internal use, on condition that the copier pay the $10.00 per-copy fee to the Copyright Clearance Center, Inc., 222 Rosewood Drive, Danvers, MA 01923; include the code 0001-1452/07 $10.00 in correspondence with the CCC.

*Assistant Research Scientist, Department of Aerospace Engineering.
†Associate Professor, Department of Aerospace Engineering.
‡Minta Martin Professor, Department of Aerospace Engineering.

The process of tip vortex formation and rollup from a helicopter rotor blade is extremely complicated because the flowfield is turbulent, three-dimensional, and involves high pressure and velocity gradients. It is well understood that the pressure difference between the lower and upper surfaces of the blade accelerates the flow from the lower surface around its tip. This, combined with the freestream flow, results in the formation of a tip vortex. However, this is an inviscid description and it masks the intricate details of the flow physics. In practice, the viscous nature of the flow coupled with the local pressure gradients causes multiple crossflow separations near the tip surface [1,2]. As a consequence, secondary and tertiary vortical structures are formed. These structures continue to evolve on the upper surface and ultimately merge into a coherent vortex structure downstream of the blade's trailing edge. In addition, part of the shear layer from behind the trailing edge is also entrained into the tip vortex flow.

Although the tip vortex is fully rolled up and largely axisymmetric in the far field [3–5], the aforementioned effects determine its initial strength and structure. Hence, it becomes imperative to understand the near-field flow physics. In the present work, high-resolution computational methodologies and experimental techniques are used synergistically to further the understanding of tip vortex formation and rollup from a hovering rotor blade.

The accurate numerical simulation of the tip vortex flowfield is a difficult task because of numerical and turbulence modeling errors. At the Reynolds numbers typical of flight applications, direct and large eddy simulations prove to be prohibitively expensive and Reynolds-averaged Navier–Stokes (RANS) solution is the only viable option. Numerical errors (dispersion and dissipation) can be reduced, or at least quantified, by using high-resolution numerical schemes and fine grids. RANS turbulence modeling errors are, in practice, more challenging to resolve. The tip vortex flowfield typically involves multiple coherent structures and separated flow regions. Although none of the available turbulence models have proven to be comprehensive enough to handle these effects, it has been shown [2] that reasonable predictions of the mean flowfield can be expected, often to within acceptable engineering accuracy. The fidelity of modeling the exact blade geometry and application of the correct boundary conditions can also affect the predictive accuracy.

Experimental measurements involve different issues. It is difficult to use an intrusive technique such as hot-wire anemometer (HWA) for rotor measurements, mostly because of proximity issues to the blades. Also, the spatial resolution offered by HWA is not sufficient

to resolve the vortex flowfield accurately. Even though nonintrusive measurement techniques such as laser Doppler velocimetry (LDV) can sufficiently resolve a given flowfield (spatially and temporally), the time required to make a given set of measurements is substantial. Additionally, optical access and measurement uncertainty are always an issue. Particle image velocimetry (PIV) is much faster than LDV and has the advantage of being a whole-plane measurement technique. However, PIV is more sensitive to calibration errors and can suffer from spatial resolution issues if large regions of the flow are to be interrogated.

Although experimental [1,6] and computational [7–9] studies of fixed-wing vortex formation are available in the literature, similar work on rotary-wing vortex formation is found to be lacking using either approach. Numerous measurements have been made in the past to understand the evolutionary characteristics of rotating blade tip vortices [3,10–13], however, none of these experiments have examined the on-blade formation of the vortices.

The ultimate objective of this work is to establish a benchmark experimental data set and also a RANS computational solution of the initial stages of tip vortex formation and rollup from a rotating blade. Given the inherent deficiencies of simple RANS models, an assessment is made of its predictive capabilities. In addition to enhancing the understanding of tip vortex formation, the new knowledge of the flowfield is expected to help in the design of tip shapes that are aimed at reducing induced losses and mitigating the strength of the tip vortex in an efficient manner.

## Test Case

The test case corresponds to a single-bladed hovering rotor, previously investigated by Martin et al. [3]. Originally, tip vortex *evolution* was studied using LDV-based velocity measurements made at selected wake planes ranging from wake ages of 3 to 395 deg. The setup consisted of a single untwisted blade with rectangular planform (with a square tip shape) operated on a hover test stand. The relevant test-case details are given in Table 1. The resulting rotor thrust coefficient for the test runs was approximately 0.002.

## Computational Methodology

The computations were performed using the compressible RANS code OVERTURNS [2]. The inviscid terms were computed using the fifth-order weighted essentially nonoscillatory (WENO) scheme [14] with Roe's flux difference splitting. The viscous terms were computed using fourth-order central differencing. The equations were solved in a rotating reference frame, such that only a steady-state solution is sought. The Spalart–Allmaras (S–A) [15] turbulence model was used to close the RANS equations. The convergence of the numerical solution was ensured by verifying that the variation in the total computed thrust was less than 1% and the total residual dropped by at least four orders of magnitude from the initial condition for both the flow solver and turbulence model.

Many experimental [1,4,16] and analytical [17] studies on tip vortices have reported largely reduced turbulence levels inside the vortical core. This has been attributed to the near-solid body rotation that prevails inside the core. It is well known [18] that linear eddy viscosity closures cannot model this behavior implicitly. Hence, such models have to be modified to account for this effect. A simple correction to the production term initially suggested in [9] is used to represent this phenomena. In this method, the production term is given by $S = |\omega| + C_{\text{prod}} \min(0, |\mathrm{D}| - |\omega|)$, where $|\omega|$ and $|D|$ are the magnitudes of the vorticity and strain tensors, respectively, and $C_{\text{prod}} = 2.0$. This formulation attempts to suppress the turbulence production in regions (such as tip vortices) in which the vorticity is much larger than the strain rate. The modification will be passive in thin shear layers in which the magnitudes of the strain rate and vorticity are roughly equivalent. It should be noted that if $C_{\text{prod}} = 0$, the baseline S–A model is recovered.

**Table 1 Experimental test conditions**

| | |
|---|---|
| Blade chord | 44.5 mm |
| Aspect ratio | 9.12 |
| Tip Mach number | 0.26 |
| Tip Reynolds number | 272,000 |
| Collective pitch | 4.5° |
| Root cutout | 20% |
| Airfoil | NACA 2415 |

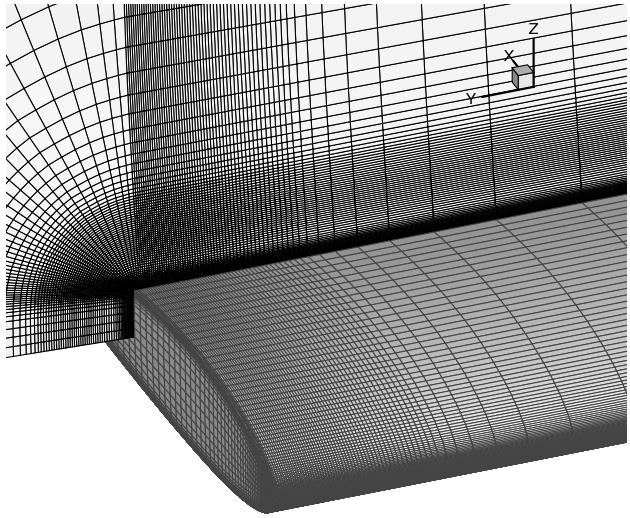


**Fig. 1 Sample section of blade mesh used in the computation.**

A two-mesh-overset system was used with a body-conforming blade mesh and a cylindrical background mesh. The blade mesh is of a C–O topology, such that both the tip and root vortices are resolved. The region of tip vortex formation is very finely resolved in the blade mesh, with a mesh spacing of $0.0025c$ in the cross-stream direction (Fig. 1). Three different mesh sizes were used to ascertain grid convergence. The finest mesh consisted of 313 points in the streamwise wraparound direction, 137 in the spanwise direction, and 109 in the normal direction. The coarser mesh used half the number of points in the wraparound direction, and the coarsest mesh used half the points in all three directions. The streamwise planes in the wake region of the blade mesh were curved to keep the flow features aligned with the mesh lines. This also provides a good overlap region for improved interpolation on to the background mesh.

To account for the far-field boundaries (note that in the present work, the objective was just to study the near-blade vortex formation and not its far-field evolution), a cylindrical background grid was used. Throughout the first revolution of the vortex, a cross-stream spacing of $0.01c$ was maintained (Fig. 2). The azimuthal spacing was fine (0.5 deg) in the region of the blade and coarser elsewhere. The radial outer boundary is at $2.5R$ and the top and bottom boundaries are at 1.5 and $3.0R$, respectively. At the outer boundaries of the background grid, the point-sink/momentum-theory characteristic boundary condition [19] was used. Periodicity was imposed along the first and last azimuthal planes. The dimensions of the background grid were $187 \times 211 \times 223$ in the azimuthal, spanwise, and vertical directions, respectively.

## PIV Experimental Setup

The rotor was tested in the hovering state in a specially designed flow-conditioned test cell [13]. The entire test area, including the flow at the rotor, was uniformly seeded with a thermally produced mineral oil fog, with particles of about 0.2 to 0.22 $\mu$m in diameter. The size of the seed particle was large enough to reflect the laser light for particle/pattern identification by the charge coupled device (CCD) camera, but small enough to minimize the particle tracking errors for the vortex strengths [20]. Even though the size of the particle image was slightly smaller than the pixel size of the camera, no pixel locking errors were observed [21].

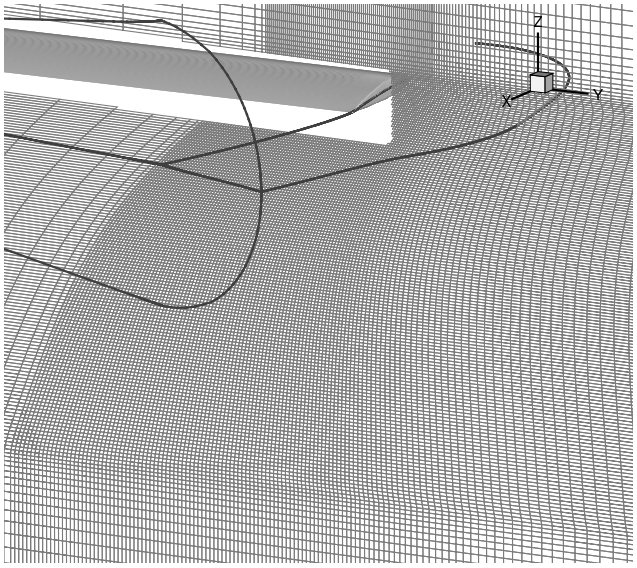


**Fig. 2 Sample azimuthal section view of background mesh; blade grid boundaries are also shown.**

The PIV system for the current experiment included a dual-pulsed Nd:YAG laser source that was pulsed in synchronization with the rotational frequency of the rotor. Two different sets of camera systems were used: one for diagnosing the flow around the rotor blade, for which a two-mega-pixel digital CCD camera was placed orthogonally to the laser light source, and another for measuring the strength of a fully formed vortex at 3 deg of wake age, for which two two-mega-pixel digital CCD cameras were used and oriented to satisfy the Scheimpflug criteria. These configurations correspond to two-component (2-C) and stereoscopic three-component (3-C) PIV, respectively (see Fig. 3). Along with this, a high-speed digital frame grabber and PIV analysis software were also used.

For the 2-C PIV, a laser pulse separation time of 1 $\mu$s was used. This corresponds to less than 0.015 deg of blade motion. The region of focus was limited to 30 by 26 mm and was interrogated using 65 by 65 nodes on either side. This corresponded to an interrogation size of 0.46 by 0.4 mm between adjacent nodes. Such a high resolution is essential to resolve the small-scale vortical structures present in this case. Adaptive grid correlation with an interrogation window size of approximately 24 pixels on either side with 0% overlap was used for this analysis.

In the case of 3-C PIV, a pulse separation time of 0.8 $\mu$s was used. A deformation grid, which also shears the interrogation window (instead of a simple shifting) to account for high-velocity gradients, was used in conjunction with a fast Fourier transform correlation and three-point Gaussian for correlating the images and estimating the velocity peak, respectively. An interrogation window size of 8 by 8 pixels with 50% overlap was used. The entire procedure, starting from calibration to processing the images and estimating the errors associated with all the individual processes, is given in detail in [21].

## Results

Figure 4a shows the computed spanwise lift distribution (scaled by local Mach number, to present an idea of the bound circulation) over the blade. Because the blade is untwisted, it is tip-loaded and, hence, a strong tip vortex can be expected even at such relatively low thrust levels. As seen from Fig. 4b, the presence of the tip vortex causes sharp gradients in the lift distribution.

Figure 5a shows the computed contours of streamwise vorticity at selected streamwise sections of the blade. Note that $\psi = 0$ deg would correspond to a plane that passes through the hub and the trailing edge of the blade tip. Because of the pressure difference between the top and bottom surfaces, a flow is induced to curl over the tip toward the top surface. The viscous nature of the flow causes a crossflow boundary layer, and streamwise vorticity is seen to extend from the lower to the upper surface in the form of a thin vortex sheet. Upstream of the quarter-chord point, a pair of counter-rotating vortices (the upper one will be referred to as SV1 and the lower as SV2; also refer to Figs. 6 and 7) are formed at each edge of the tip. These vortices are formed as a result of the crossflow separation that is caused by the sharp surface edges. Good correlation can be observed between the computational predictions and the experiment, especially when identifying the secondary vortices.

Under normal conditions with a rounded tip blade, only one separation line can be expected, and its location will depend on the flow conditions. In the present case, the separation locations are fixed by the tip geometry. Immediately downstream of the quarter-chord point, as the driving pressure gradient weakens, this sheet of vorticity separates off the blade surface. The separated shear layer evolves into

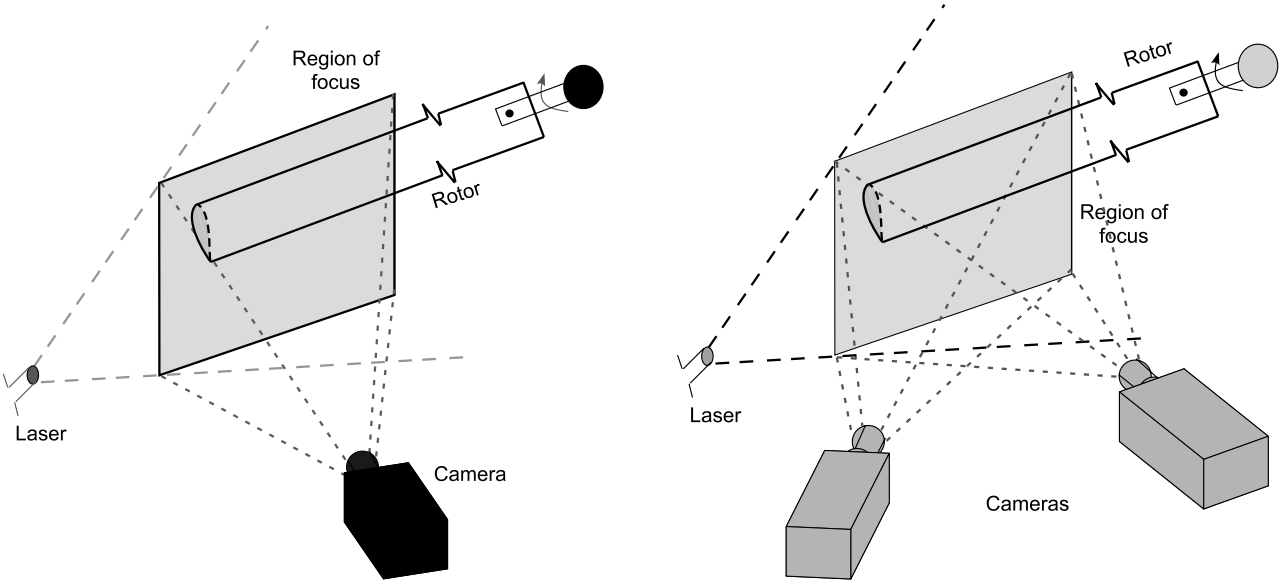


**a) 2-component PIV** **b) 3-component PIV**

**Fig. 3 Schematic of the PIV setup.**

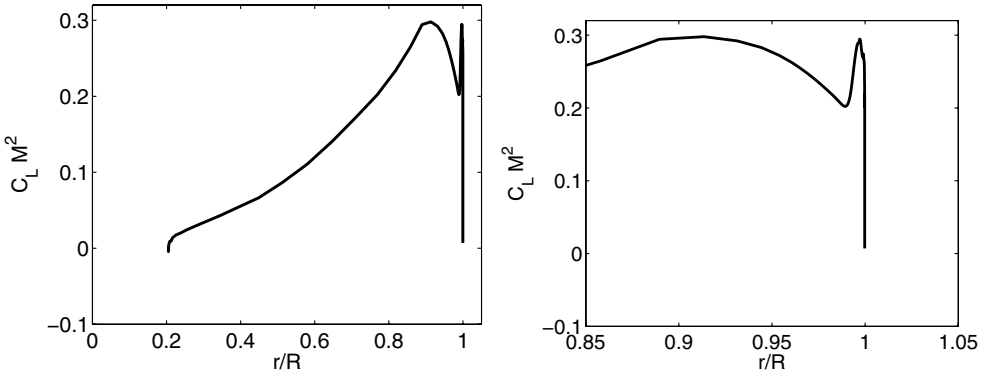


a) Full span b) Near the tip

**Fig. 4 Computed spanwise lift distribution scaled by sectional Mach number *M*.**

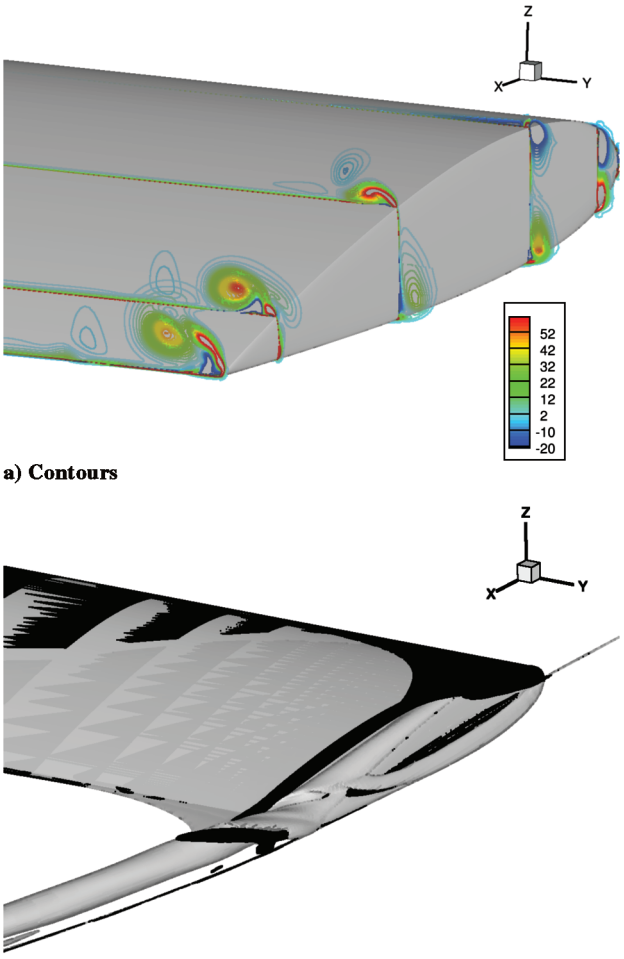


a) Contours




b) Iso surfaces (dark: $\Omega_x$ = -5, light: $\Omega_x$ = 10)

**Fig. 5 Formation of the trailed vortex system; streamwise vorticity $\Omega_x$ nondimensionalized by tip speed and chord.**

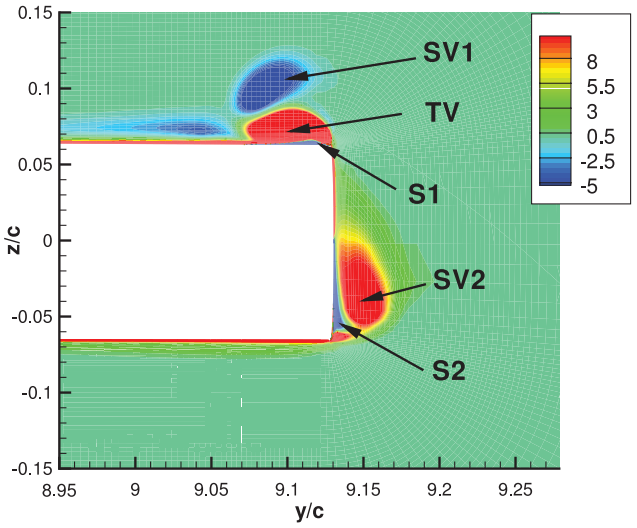


a) RANS

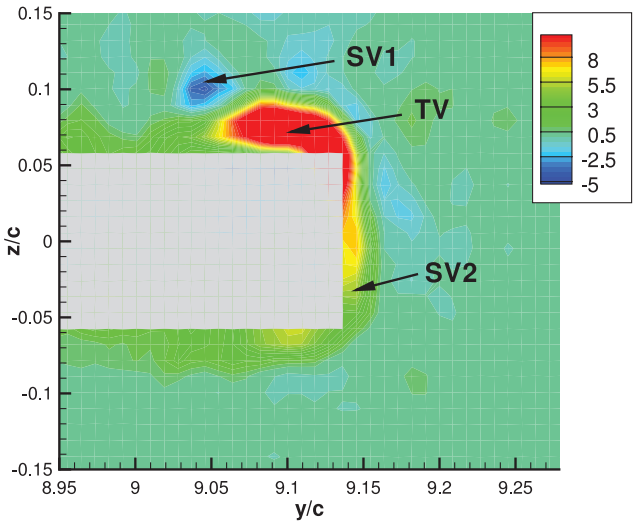


b) PIV (time-averaged)

**Fig. 6 Vortical structures in computations (RANS) and PIV (time-averaged) at $\psi = -3$ deg (approximately midchord); contours of streamwise vorticity (nondimensionalized by tip speed and chord) are shown.**

the primary tip vortex (TV) as a result of the rollup caused by its self-induced velocity. Further downstream, the TV grows in strength as the vortex sheet continues to roll up. Meantime, the sense of rotation causes the SV2 to be entrained into the TV. These structures continue to evolve, and downstream of the trailing edge of the blade, the secondary and tertiary vortices, which are now free to convect, are rapidly entrained into the TV. Subsequently, a coherent axisymmetric vortex is formed (Fig. 5b).

Figures 7 and 8 compare the computed and time-averaged measurements of the axial vorticity contours along different streamwise planes near the blade tip. The various vortical structures

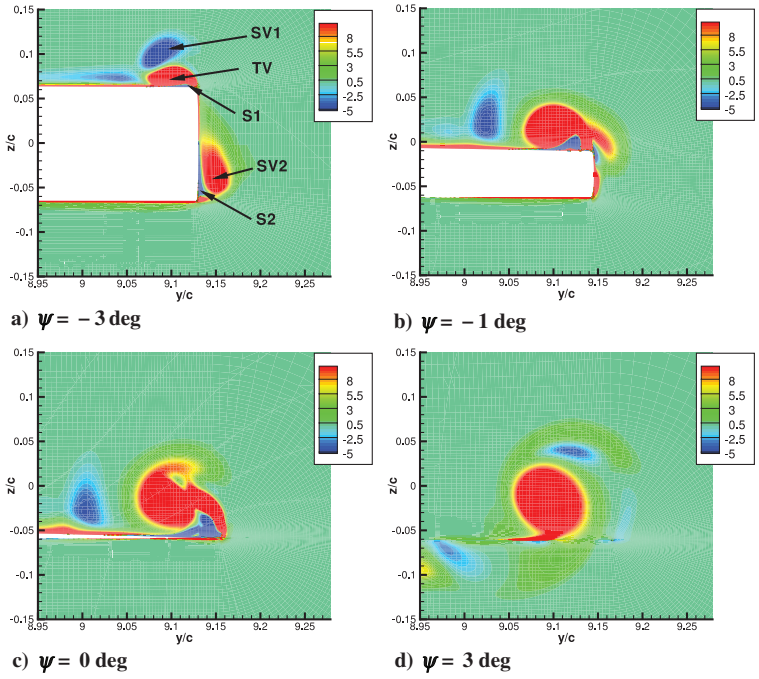


**Fig. 7 Computed streamwise vorticity (nondimensionalized by tip speed and chord) at different wake planes.**

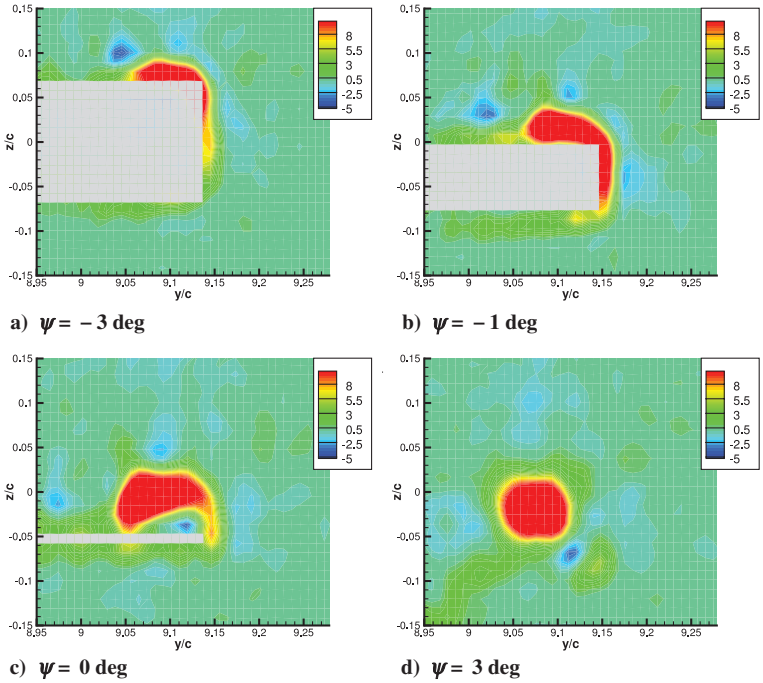


**Fig. 8 Time-averaged PIV streamwise vorticity. Blanked out area includes region larger than the blade surface.**

previously discussed are also evident in the PIV measurements. The maximum and minimum cutoff levels of the contours are chosen such that the different flow structures can be clearly discerned.

Figures 9 and 10 compare the computed and measured cross-stream velocities. For the purposes of comparison, the computed results were linearly interpolated onto the same grid that was used in the measurements. Though qualitative similarity is seen, the computed values seem to be larger in magnitude.

Two important distinctions need to be recognized. First, the PIV reports instantaneous measurements that are ultimately phase-averaged over many rotor revolutions. The character of the flowfield (especially the secondary structures) was found to be unsteady (aperiodic) and, hence, comparison with a steady RANS computation cannot be direct because phase-averaging of different planes of strobed PIV data tends to smear out the unsteady vortical structures [13]. Second, the spatial resolution in the computation is almost 10 times higher than that in the PIV (the discrete measurement grid can be identified with the origin of the crossflow velocity vectors). Hence, significant issues can be expected to arise in the identification of small flow structures, the intensity of the vorticity, and other flow gradients.

For the purposes of further validation, the computed and PIV velocity profiles downstream of the trailing edge of the blade are compared with the LDV measurements of Martin et al. [3] on the same test setup (the earliest available wake age reported in the LDV data set is $\psi = 3$ deg). The magnitude of peak swirl velocity

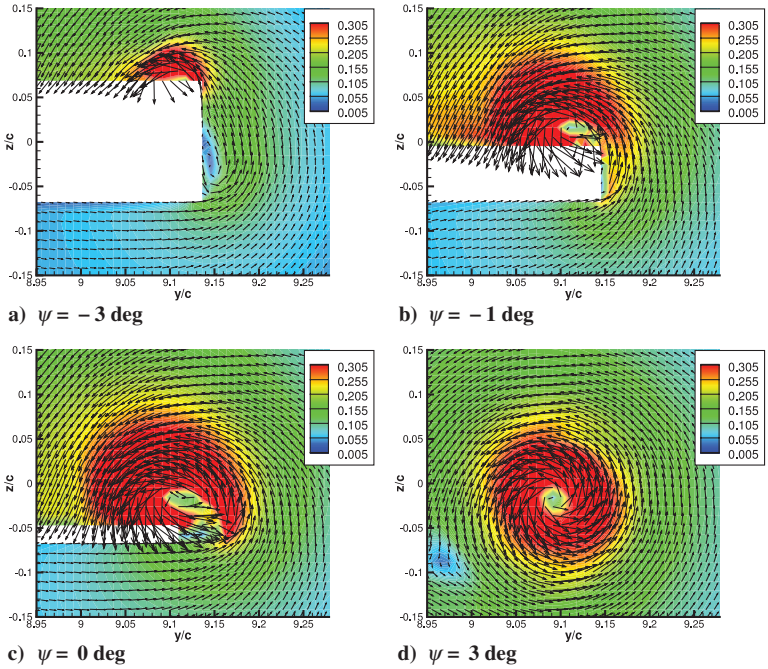


**Fig. 9 Computed velocity vectors and magnitudes (contours).**

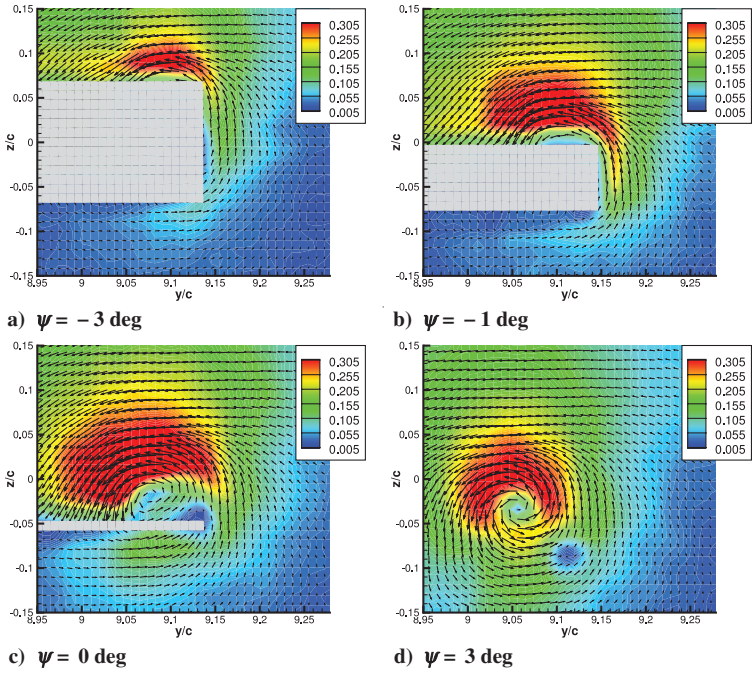


**Fig. 10 Time-averaged PIV velocity vectors and magnitudes (contours).**

predicted by computational analysis appears to be larger than both the PIV and LDV measurements (see Fig. 11a). This underprediction may be attributed to the simple phase-averaging that was used in both the LDV and PIV measurements.

Although the computational predictions show the peak swirl velocity to be around 38% of the blade tip velocity, the PIV shows 33% and the LDV shows 30%, respectively. PIV measures higher peak swirl velocity despite having lower spatial resolution (120 $\mu$m in the case of PIV when compared with 80 $\mu$m in LDV). Away from the vortex axis, the LDV measurements are in striking agreement with the computational predictions compared with the PIV measurements (Fig. 11b).

The effect of spatial resolution can be understood from Fig. 11c. It can be observed that the measurements made using the higher spatial resolution show a higher peak swirl velocity when compared with their lower spatial resolution counterparts. This is expected, because the PIV is known to underpredict the velocity magnitude when the velocity gradient is substantial, as in the case of tip vortices. This is because of the biased correlation toward lower velocities [21]. Smaller interrogation windows are known to tolerate the velocity gradients better.

In the case of the axial velocity, the PIV shows a higher velocity deficit when compared with the LDV measurements (Fig. 12). It should be noted here that in the case of LDV the axial velocities were

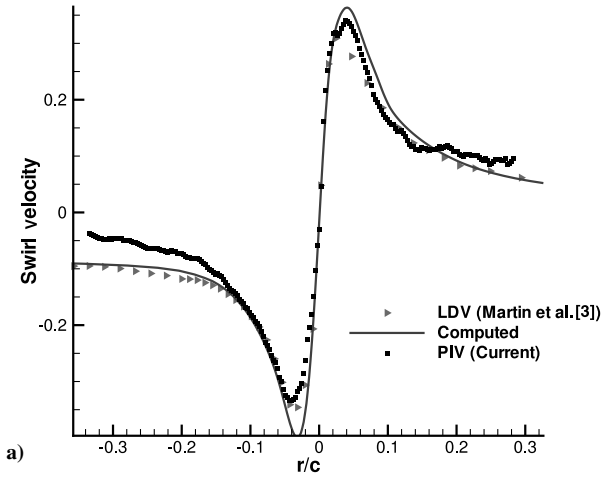


a)

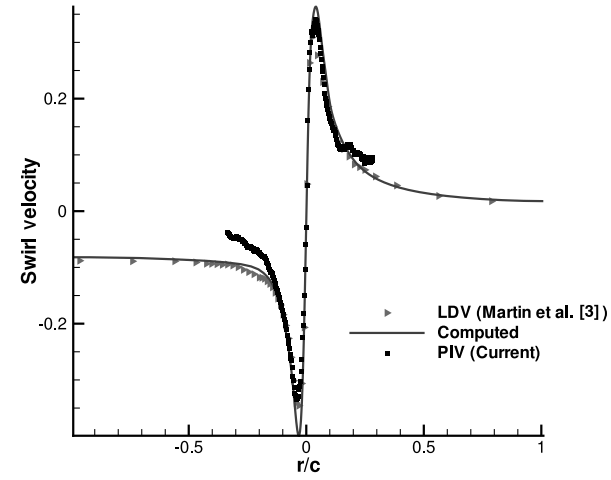


b)

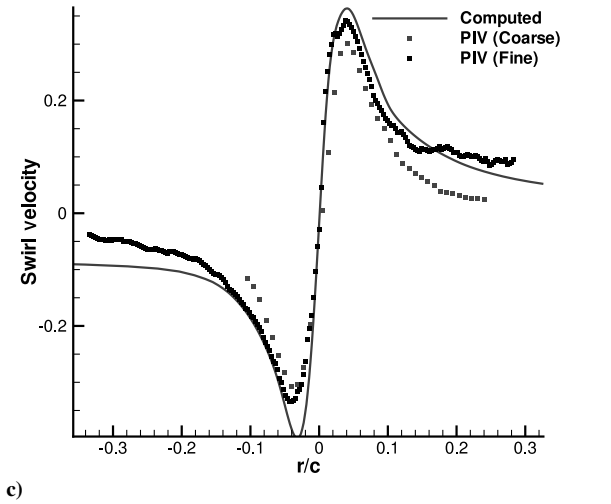


c)

**Fig. 11 Comparison of computed and measured swirl velocities along a hoizontal line passing through the vortical core at a wake age of $\psi = 3\,\mathrm{deg}$.**

measured using the on-axis configuration [3]. As a result, the spatial resolution of the measurements is not as good as the swirl velocity measurements. The correlation between the PIV measurements and the computational predictions in the axial velocity gradient is excellent. However, away from the vortex core, it can be observed that the velocity measured by PIV is not as smooth as seen in the LDV measurements. An uncertainty analysis made on these measurements can explain this [21]. It has been shown that the uncertainty in the measurements increases with a decrease in velocity or the

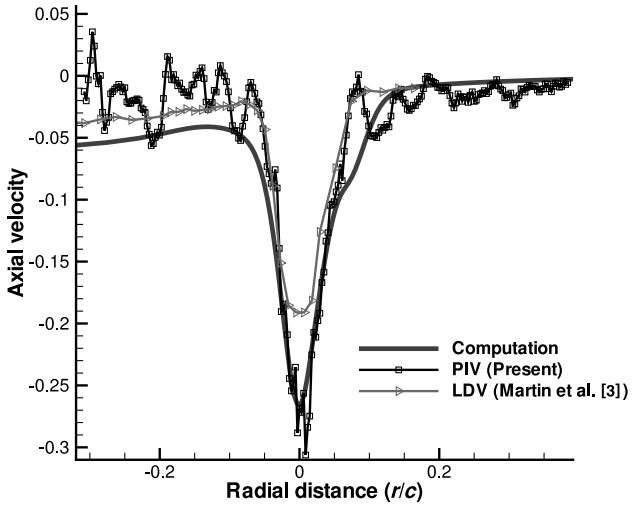


**Fig. 12 Comparison of computed and measured axial velocities along a hoizontal line passing through the vortical core at a wake age of $\psi = 3\,\mathrm{deg}$.**

displacement of the seed particles within the interrogation window. The minimum accurately measurable velocity for the present study was $\approx 4$ m/s.

The unsteady (aperiodic) behavior of the flowfield is apparent through different instantaneous PIV frames acquired at 3 deg of wake age, as shown in Fig. 13. Phase-averaging, as mentioned earlier, will smear out the measurements, resulting in an increase in the core size and a reduction in the peak swirl velocity. For a fully developed vortex, different procedures have been proposed to correct the velocity field using ensemble averaging [22] for LDV. However, no such formal methods have yet been established for PIV. Therefore, no correction was employed in the present study to maintain consistency between the LDV and PIV measurements.

## Possible Sources of Inaccuracy

### Computational Errors

Even though the nature of the flowfield is extremely complicated near the blade surface, reasonable qualitative and quantitative agreement of the predictions with the PIV was still achieved. At the earliest available wake age, the computations were also observed to compare well with LDV measurements, up to large radial distances from the vortex axis. However, computational solutions of the RANS equations suffer from numerical and turbulence modeling errors. The numerical errors are expected to be very small as a result of using highly fine meshes and high-order numerical schemes. The values of the peak-to-peak swirl velocity and maximum vorticity were found to change less than 3% between the finest and the next-coarser mesh level, thus suggesting that numerical errors are not significant. However, with the coarser mesh levels, the smaller structures appeared to be dissipated, as shown in Fig. 14, which corresponds to the results from the coarsest mesh (half of the points in each direction). The fact that in their initial formation stages the secondary structures are more than an order of magnitude smaller than the evolved tip vortex, suggests that true mesh independence would be very difficult to achieve (heuristically, accurate resolution of a coherent flow structure would require around 15 points across its length). Compared with the numerical errors, which are dependent on the discretization, several sources of error can be expected from the turbulence modeling:

1) Linear eddy viscosity assumption: It is well known that tip vortex flowfields are anisotropic [9,23]. Therefore, the use of linear eddy viscosity models will introduce significant errors into the turbulent quantities. However, this will not necessarily affect the mean flow quantities in a significant manner.

2) Rotational correction: In this work, to account for streamline curvature, a simple correction was made to the production term of the

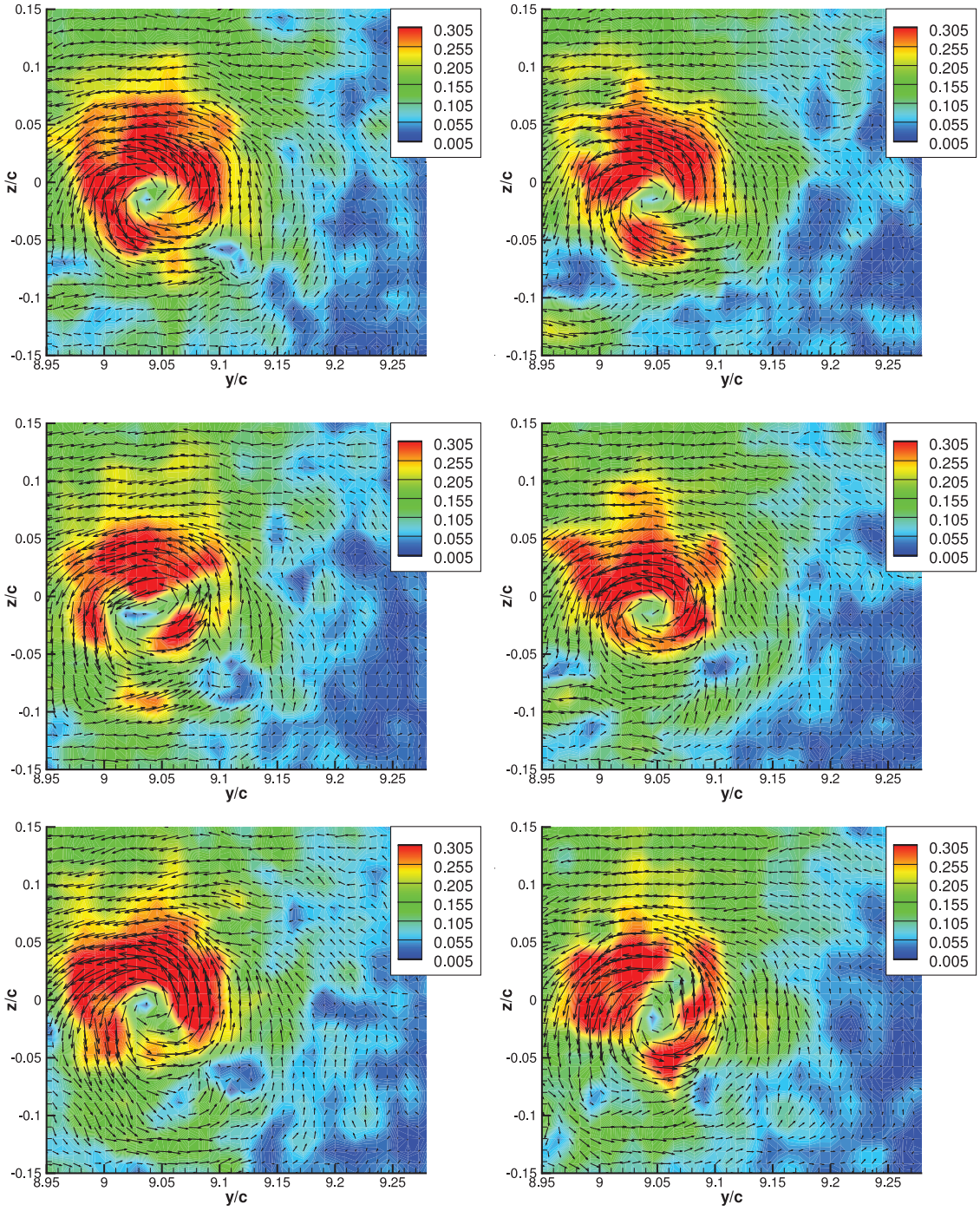


**Fig. 13 Sample instantaneous PIV shots of velocity vectors and magnitudes (contours) at $\psi = 3\,\mathrm{deg}$.**

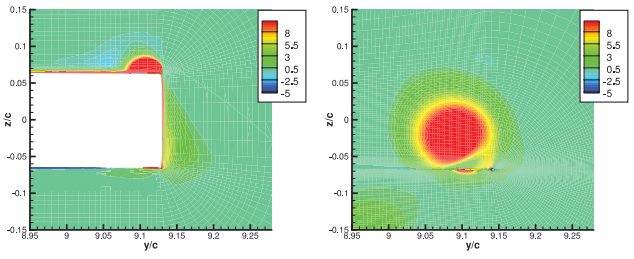


**a) $\psi = -3$ deg** **b) $\psi = 3$ deg**

**Fig. 14 Contours of streamwise vorticity on the coarsest mesh.**

turbulence model (as mentioned earlier in the paper). However, this correction is not rigorous and is a continuing area of development in turbulence modeling [18]. Several ideas are usually adapted from higher-order models to improve the linear eddy viscosity models.

3) RANS closure: The present flowfield is a prime example of a nonequilibrium flow. A nonequilibrium flow is characterized by multiple length scales and a lack of balance between the production and dissipation of turbulence. No turbulence model has been proven to be successful in comprehensively describing flowfields that are as complicated as the presently considered case.

4) The nature of RANS equations: The RANS equations are solved in the present computations. However, given the multiple small-scale structures and the unsteadiness of the flowfield, the very assumption of steady Reynolds averaging is questionable to an extent because some of the smaller-scale, possibly unsteady,

structures are being computationally resolved. A first step would be to increase the spatial resolution and verify whether the time-accurate solution tends to be unsteady.

#### Measurement Errors

Comparing the results from the measurements obtained from the PIV and the predictions from the RANS solution immediately points to the resolution required to resolve the coherent small-scale structures present in the rotor flowfield. The realization of SV2 and SV3 was possible in the present measurements because of the increased spatial resolution. Even though their presence has been identified, the measurements show a lower magnitude in vorticity and velocity compared with the RANS solution. This is despite reducing the region of focus in the flow to approximately 1 in. by 1 in. Unfortunately, this also begins to negate the advantage of using PIV because of the need to move the entire setup to measure the flow at every few wake ages.

These errors are a result of the combination of various factors: The fundamental principle of two-dimensional PIV is to acquire two images of the seed particles present in the region of focus during a specified time interval (pulse separation time). These images are then divided into smaller regions (called interrogation windows) for correlation through particle or pattern identification. The correlation between the images gives the absolute displacement of the particles within each interrogation window. This displacement, upon division by time, gives the velocity magnitudes. This technique will yield accurate velocity magnitudes for an irrotational flowfield. However, in a rotational flow such as a tip vortex flow, the streamline curvature induced by the tip vortex brings the complication that the seed particles follow a circular path with decreasing curvature for increasing radial distance from the center of the vortex. This curvature information is lost in PIV when two images that are acquired within a small time interval are analyzed to find the velocity magnitudes. The only stored information is the initial and final spatial positions of the particle.

As a result, the displacement of particles in PIV is estimated as the smallest distance traveled by the particle between the two acquired images. This error can be reduced by reducing the pulse separation time. It is apparent from the results in Fig. 15 that the reduction in the pulse separation time does result in a decrease of the error. However, a reduction in pulse separation time also decreases the distance traveled by the seed particles. This is especially true in the far field, in which the swirl velocities are relatively small. This can introduce correlation errors because the pulse separation time (and, hence, the seed particle displacement) is optimized for accurately measuring the peak swirl velocity. This can, in part, explain the discrepancy between the LDV and PIV in the far field, as seen in Fig. 11. Additionally, the reduction in pulse separation time can also reduce the errors associated with the presence of accelerations in the flowfield [21]. A detailed discussion on the various errors and uncertainties associated with using PIV for vortex flows is given in [21].

The difference in the velocity profile between the LDV and PIV measurements may be attributed, in part, to the unsteady nature of the flowfield. At 3 deg of wake age, the center of vorticity moved aperiodically in a random fashion, as evidenced in Fig. 13. The measured standard deviation in the swirl and axial components of velocity from this aperiodic spatial movement of the tip vortices is shown in Fig. 16. The axial velocity shows fluctuations that are of the order of the mean peak deficit itself. Even though both the PIV and LDV techniques phase-average the velocity values and the results are not corrected for this aperiodicity, the number of samples obtained by PIV is far less than that of LDV. In the case of PIV, 50 images were phase-averaged. The LDV measurements used at least 500 data points for each measurement point. Clearly, an increase in the number of samples could reduce this discrepancy.

## Conclusions

An investigation into the physics of vortex formation from a single-bladed hovering rotor was performed. The high resolution of both the computation and experiments allowed for an unprecedented level of detail. The computation used high-order numerical schemes on a very fine grid with a simple correction to the turbulence model to account for streamline curvature effects. The region of focus in the PIV was interrogated using a $64 \times 64$ mesh within a square of just $0.5c$ times the chord length (corresponding to a 1-in. square). Distinct multiple vortex structures were identified and were found to ultimately merge into a single coherent tip vortex. Good agreement was achieved between the numerics and the experimental data, even though a simple linear eddy viscosity model was used as the RANS closure. It is expected that the present data set will prove to be a useful validation tool with future advances in RANS/LES and experiments.

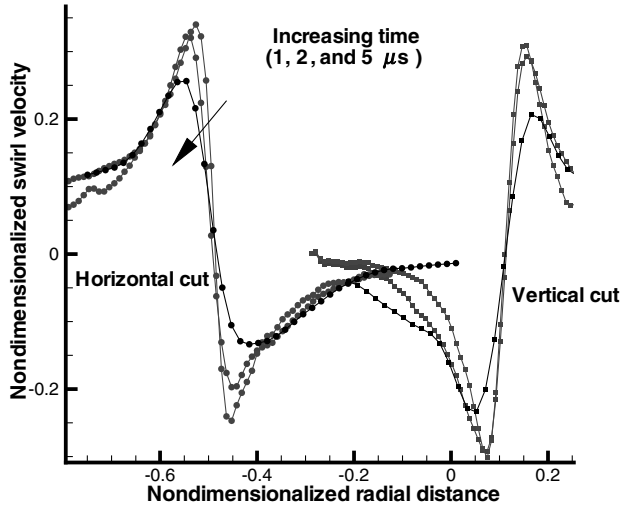


**Fig. 15 Effect of pulse separation time on velocity measurements; velocity profiles normal to cuts along the center of the core at $\psi = 3$ deg.**

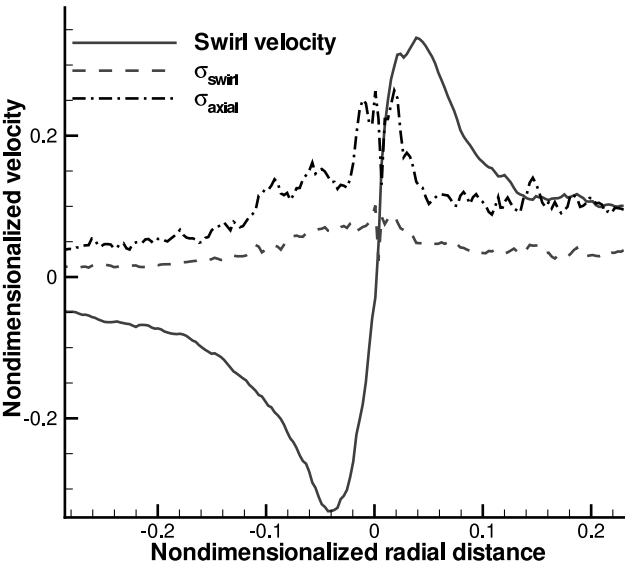


**Fig. 16 Measured scatter of swirl and axial velocity components across at $\psi = 3$ deg.**

## Acknowledgments

This work was conducted at the Alfred Gessow Rotorcraft Center at the University of Maryland, and supported, in part, by the National Rotorcraft Technology Center under grant NCC 2944.

## References

[1] Chow, J. S., Zilliac, G. G., and Bradshaw, P., "Mean and Turbulence Measurements in the Near Field of a Wingtip Vortex," *AIAA Journal*, Vol. 35, No. 10, 1997, pp. 1561–1567.

[2] Duraisamy, K., "Studies in Tip Vortex Formation, Evolution and Control," Ph.D. Dissertation, Dept. of Aerospace Engineering, Univ. of Maryland, College Park, MD, Apr. 2005.
[3] Martin, P. B., Pugliese, G., and Leishman, J. G., "High Resolution Trailing Vortex Measurements in the Wake of a Hovering Rotor," *Journal of the American Helicopter Society*, Vol. 49, No. 1, 2003, pp. 39–52.
[4] Devenport, W. J., Rife, M. C., Liapis, S. I., and Follin, G. J., "The Structure and Development of a Wing-Tip Vortex," *Journal of Fluid Mechanics*, Vol. 312, 1996, pp. 67–106. doi:10.1017/S0022112096001929
[5] Ramasamy, M., "Contributions to the Measurement and Analysis of Helicopter Blade Tip Vortices," Ph.D. Thesis, Dept. of Aerospace Engineering, Univ. of Maryland, College Park, MD, Sept. 2004.
[6] Birch, D., Lee, T., Mokhtarian, F., and Kafyeke, F., "The Structure and Induced Drag of a Tip Vortex," *Journal of Aircraft*, Vol. 41, No. 5, 2004, pp. 1138–1145.
[7] Duraisamy, K., Sitaraman, J., and Baeder, J. D., "High Resolution Computational Methodology for Improved Rotor Aerodynamic Calculations," *61st Annual Forum Proceedings of the American Helicopter Society* [CD-ROM], AHS International, Alexandria, VA, June 2005.
[8] Churchfield, M. J., and Blaisdell, G. A., "Near Field Wingtip Vortex Computation Using the WIND Code," 44th AIAA Aerospace Sciences Meeting and Exhibit Proceedings, Reno, NV, AIAA Paper 2006-633, Jan. 2006.
[9] Dacles-Mariani, J., Chow, J. S., Zilliac, G. G., and Bradshaw, P., "Numerical/Experimental Study of a Wingtip Vortex in a Near Field," *AIAA Journal*, Vol. 33, No. 9, 1995, pp. 1561–1568.
[10] Cook, C. V., "The Structure of the Rotor Blade Tip Vortex," *AGARD Conference Proceedings*, CP-111, AGARD, London, Sept. 1972, Paper 3.
[11] Tung, C., Pucci, S. L., Caradonna, F. X., and Morse, H. A., "The Structure of Trailing Vortices Generated by Model Helicopter Rotor Blades," NASA TM 81316, 1981.
[12] McAlister, K., "Rotor Wake Development During the First Rotor Revolution," *59th Annual Forum Proceedings of the American Helicopter Society* [CD-ROM], AHS International, Alexandria, VA, May 2003.
[13] Ramasamy, M., and Leishman, J. G., "Interdependence of Diffusion and Straining of Helicopter Blade Tip Vortices," *Journal of Aircraft*, Vol. 41, No. 5, 2004, pp. 1014–1024.
[14] Shu, C-W., "Essentially Non-Oscillatory and Weighted Essentially Non-Oscillatory Schemes for Hyperbolic Conservation Laws," Inst. for Computer Applications in Science and Engineering Rept. 1997-65, 1997.
[15] Spalart, P. R., and Allmaras, S. R., "A One-Equation Turbulence Model for Aerodynamic Flows," 30th AIAA Aerospace Sciences Meeting and Exhibit Proceedings, Reno, NV, AIAA Paper 92-0439, Jan. 1992.
[16] Ramasamy, M., and Leishman, J. G., "A Generalized Model for Transitional Blade Tip Vortices," *Journal of the American Helicopter Society*, Vol. 51, No. 1, 2006, pp. 92–103.
[17] Jacquin, L., and Pantano, C., "On the Persistence of Trailing Vortices," *Journal of Fluid Mechanics*, Vol. 471, Nov. 2002, pp. 159–168. doi:10.1017/S0022112002002161
[18] Jakirlic, S., Hanjalic, K., and Tropea, C., "Modeling Rotating and Swirling Turbulent Flows: A Perpetual Challenge," *AIAA Journal*, Vol. 40, No. 10, 2002, pp. 1984–1996.
[19] Srinivasan, G. R., Baeder, J. D., Obayashi, S., and McCroskey, W. J., "Flowfield of a Lifting Rotor in Hover: A Navier–Stokes Simulation," *AIAA Journal*, Vol. 30, No. 10, 1992, pp. 2371–2378.
[20] Leishman, J. G., "Seed Particle Dynamics in Tip Vortex Flows," *Journal of Aircraft*, Vol. 33, No. 4, 1996, pp. 823–825.
[21] Ramasamy, M., and Leishman, J. G., "Benchmarking PIV with LDV Measurements in the Wake of a Hovering Rotor," 25th Applied Aerodynamics Conference Proceedings, San Francisco, CA, AIAA Paper 2006-3479, June 2006.
[22] Leishman, J. G., "On the Aperiodicity of Helicopter Rotor Wakes," *Experiments in Fluids*, Vol. 25, No. 4, 1998, pp. 352–361. doi:10.1007/s003480050240
[23] Zeman, O., "The Persistence of Trailing Vortices: A Modeling Study," *Physics of Fluids*, Vol. 7, No. 1, 1995, pp. 135–143. doi:10.1063/1.868734

K. Fujii
*Associate Editor*